PAPER

Mode-mixing-induced second harmonic A0 mode Lamb wave for local incipient damage inspection

IOP Publishing Smart Materials and Structures
Smart Mater. Struct. 29 (2020) 055020 (12pp) https://doi.org/10.1088/1361-665X/ab7e37

Mode-mixing-induced second harmonic A0 mode Lamb wave for local incipient damage inspection

Shengbo Shan[1,2,3] and **Li Cheng**[1,2,3]

[1] Department of Mechanical Engineering, The Hong Kong Polytechnic University, Kowloon, Hong Kong, People's Republic of China
[2] The Hong Kong Polytechnic University Shenzhen Research Institute, Shenzhen 518057, People's Republic of China
[3] Hong Kong Branch of National Rail Transit Electrification and Automation Engineering Technology Research Center, The Hong Kong Polytechnic University, Kowloon, Hong Kong, People's Republic of China

E-mail: li.cheng@polyu.edu.hk

Received 28 November 2019, revised 21 February 2020
Accepted for publication 10 March 2020
Published 1 April 2020

Abstract

This paper reports the discovery of a special type of second harmonic A0 mode Lamb wave, which is generated through the mixing of primary S0 and A0 mode Lamb waves in a PZT-activated weakly nonlinear plate. Owing to the different propagating velocities of the S0 and A0 waves and the finite duration of their corresponding tone-burst wave packets, wave mixing takes place within a confined area which can be precisely controlled by tuning the wave excitation durations. When local incipient damage falls into the mixing zone, this second harmonic A0 mode wave provides higher damage detectability than the commonly used second harmonic S0 mode wave resulting from the global material nonlinearity. Moreover, through a tactic tuning of the mixing zone size, damage detection can be carried out zone by zone along the transmitter–receiver path to achieve damage localization. Finite element (FE) simulations are first carried out to ascertain the theoretically predicted phenomenon and the underlying generation mechanism of the second harmonic A0 mode Lamb waves. Capitalizing on its mode mixing feature between the primary A0 and S0 mode Lamb waves, a dedicated damage localization strategy alongside the corresponding algorithm is then proposed. Experiments are finally carried out with a dedicatedly designed inspection system with mitigated non-damage-related nonlinear interference. Both FE and experimental results demonstrate the appealing characteristics and the potential of the second harmonic A0 mode Lamb waves for local incipient damage detection and localization.

Keywords: mode mixing, second harmonic Lamb waves, incipient damage localization

(Some figures may appear in colour only in the online journal)

1. Introduction

Inspection of incipient damage in thin-walled structures is an important issue for various applications in aerospace, nuclear and automotive industries, etc, which, in turn, facilitates maintenance decisions and enhances structural integrity [1]. In virtue of their high sensitivity to material microstructural changes, nonlinear guided waves show promise for incipient damage inspections [2–6].

So far, two types of nonlinear guided wave phenomena corresponding to the material nonlinearity have been widely explored: second harmonic generation [7–9] and nonlinear wave mixing [10–14]. For the former, most existing studies focus on a single primary wave propagating in a nonlinear waveguide to generate a nonlinear component at the double of the primary wave frequency due to its self-interaction [15–20]. Through evaluating the power flux from the primary to the secondary wave components, it has been shown that the

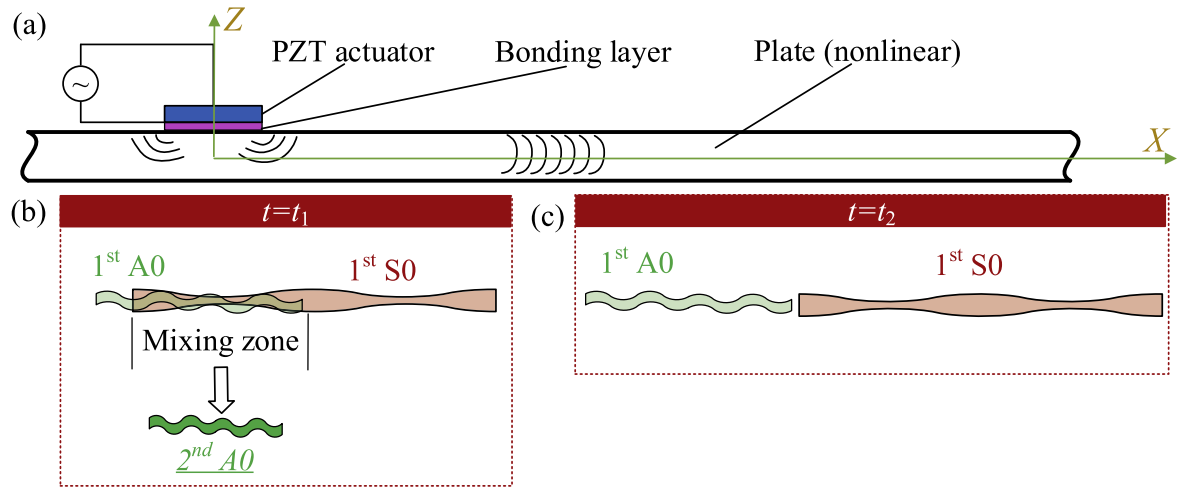

Figure 1. (a) Schematic of the PZT-driven system; (b) characteristics of nonlinear wave generation at the beginning ($t = t_1$) when the 1st A0 and S0 waves mix in the plate; (c) characteristics of nonlinear wave generation as time goes on ($t = t_2$) when the 1st A0 and S0 waves separate in the plate.

second harmonic waves should be symmetric Lamb waves, no matter whether the single primary waves are symmetric or anti-symmetric Lamb or SH waves [21–24]. For the latter, existing work investigates the mixing of two guided waves, usually at two different frequencies, to generate a nonlinear wave component at the sum or difference of the two frequency components as a result of their mutual interaction [12, 13, 25]. Based on these wave phenomena, experiments have been designed to detect various types of incipient damage caused by plasticity [26], fatigue [27], creep [28], thermal degradation [29], etc, rather than their localizations.

As an advanced level to the detection, damage localization is an important issue in structural health monitoring for further structural safety assessment and maintenance decision masking [30]. Unfortunately, in the open literature, research on the incipient damage localization with nonlinear guided waves is relatively scarce [25, 31, 32]. Among some existing works, Hong *et al* introduced a probabilistic imaging algorithm based on the analyses of the temporal information of the scattered second harmonic Lamb waves to locate fatigue cracks in an aluminum plate [31]. However, fatigue cracks usually have strong wave-scattering feature due to the contact acoustic nonlinearity. For the distributed material nonlinearity, the second harmonic responses are a result of the averaged effect over the transmitter–receiver path, which compromises the sensitivity of local damage detection and makes it extremely difficult for damage localization. Boccardi *et al* used second harmonic Lamb waves to locate material flaws in a composite plate based on a multi-path scheme [32]. However, the localization resolution of such a method highly relies on the density of the transducers. In addition, with the use of multi-paths, a switching module is required to activate different paths to achieve an automatic inspection, which sets up a harsh requirement on the system. Cho *et al* investigated the mutual guided wave mixing technique and showed that incipient damage localization can be realized by adjusting the mixing zone [25]. However, damage localization algorithms as well as the corresponding applications are still lacking and yet to be demonstrated. In addition, the two independent wave excitation channels need to be perfectly synchronized, which is quite demanding for equipment in real applications.

In this work, by examining a PZT-activated plate system where multiple primary wave modes coexist, we discover a second harmonic A0 mode Lamb wave (2nd A0 wave) that is new to the current state-of-art of the second harmonic guided waves. The underlying generation mechanism of this 2nd A0 wave is first discussed. Finite element (FE) simulations are then carried out to verify the phenomena and show its appealing characteristics for damage inspection. Through combining a previously developed theoretical model [33] with the 2nd A0 wave-based measurements, a dedicated algorithm is proposed to achieve a high-resolution damage localization using a simple measurement system. Experiments are further carried out using a meticulously designed system in which the influences of the non-damage-related adhesive nonlinearity are mitigated. After experimentally validating the existence of the 2nd A0 wave induced by material nonlinearity, localization of thermal damage in a metallic plate is carried out with the proposed algorithm.

2. Theoretical analyses

A typical plate system activated by a surface-bonded d_{31}-type PZT is considered, as sketched in figure 1(a). Upon applying an electrical voltage on the PZT, multiple Lamb wave modes, symmetric and antisymmetric, are generated in the plate. Specifically, in the low-frequency range, only the lowest S0 and A0 mode Lamb waves exist whose displacement field can

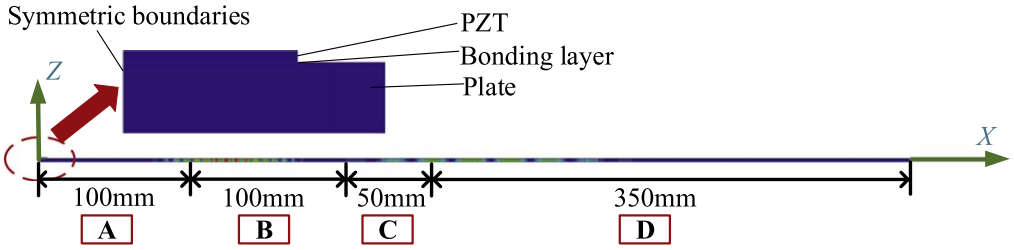

Figure 2. The finite element model.

be described as

$$\mathbf{u}_{S0/A0}(X, Y, Z) = A_{S0/A0}\mathbf{U}_{S0/A0}(Z)\exp\left(i(k_{S0/A0}X - \omega t)\right)' \quad (1)$$

where $\mathbf{U}(Z)$ depicts the displacement distribution across the plate thickness of the corresponding Lamb wave modes represented by subscript S0 and A0, respectively. A denotes the modal amplitude. k and ω stand for the wavenumber and angular frequency, respectively.

While the PZT-activated primary S0 and A0 mode Lamb waves (1st S0 and 1st A0 waves) propagate in a weakly nonlinear plate in a symbiotic manner, nonlinear Lamb waves are generated alongside the primary wave propagation. In this case, both the 1st A0 and 1st S0 Lamb waves generate the second harmonic S0 mode Lamb waves (2nd S0 waves) as a result of their self-interactions, as demonstrated in our previous work [33]. In addition, the mutual interaction between the 1st A0 and 1st S0 waves also takes place for the nonlinear wave generation, which is to be highlighted hereafter. Note the aforementioned phenomenon can be regarded as a special case of the nonlinear wave mixing but with two primary components at the same frequency. Without losing generality, the well-developed normal mode expansion [12] method can be used to describe this mutual interaction process with the resultant wave field described as

$$\boldsymbol{u}_{(S0,A0)} = \frac{1}{2}\sum_{m=1}^{N} A_m(X)\boldsymbol{U_m} \times (Z)\exp(-i(\omega_{A0} \pm \omega_{S0})t) \quad (2a)$$

with

$$A_m(X) = \begin{cases} \dfrac{i(f_m^{surf} + f_m^{vol})}{4P_{mm}(k_m^* - (k_a \pm k_b))}\begin{pmatrix}\exp(ik_m^*X) - \\ \exp(i(k_{A0} \pm k_{S0})X)\end{pmatrix} & if\ k_m^* \neq k_{A0} \pm k_{S0} \\ \dfrac{(f_m^{surf} + f_m^{vol})}{4P_{mm}}X\exp(i(k_a \pm k_b)X) & if\ k_m^* = k_{A0} \pm k_{S0} \end{cases}, \quad (2b)$$

where the subscripts (S0, A0) denote the mutual interaction of the 1st S0 and 1st A0 waves. P_{mm} stands for the complex power flow of the mth mode which is expected to be generated. f_m^{surf} and f_m^{vol} are the power flux from the primary waves to the secondary wave caused by the nonlinear surface traction and volume force respectively. Through analyzing the symmetric properties of the power flux, the corresponding nonlinear wave should be 2nd A0 wave [12]. This nonlinear wave generation mechanism is referred to as 'mode mixing' hereafter.

According to equation (2*b*), the amplitude of the generated 2nd A0 wave will be cumulative if the phase velocity of the of the 2nd A0 wave matches with its counterparts of the primary waves. Unfortunately, for a 2 mm thick aluminum plate used for the subsequent analyses, no mode combination can satisfy this phase matching condition in the low-frequency range (under 500 kHz), which means the 2nd A0 wave investigated in this work does not have the cumulative effect. However, as long as generated 2nd A0 wave can be measured, it can be used to characterize the material changes for damage inspection since it is directly induced by the material nonlinearity.

The feasibility of using 2nd A0 wave for damage inspection is then evaluated. In practical applications, tone burst excitation signals with finite cycles are preferred to guarantee sufficient temporal resolution for distinguishing different wave modes in the responses. As a result, the propagating A0 and S0 waves generated by PZT actuators will have finite length in space. At the initial time instant (i.e. $t = t_1$), the 1st A0 and 1st S0 waves mix in the plate to generate the 2nd A0 waves, as illustrated in figure 1(b). As time goes on (i.e. $t = t_2$), the A0 and S0 waves eventually separate in the spatial domain due to their different wave propagation velocities, which terminates the 2nd A0 wave generation when the two primary wave components are detached, as sketched in figure 1(c). Therefore, the effective wave mixing zone for the 2nd A0 wave generation is confined within a certain area surrounding the PZT actuator. If local incipient damage happens to occur in the same mixing area, the 2nd A0 wave is expected to provide higher detectability than the commonly used 2nd S0 wave which only contains an averaged damage information over the transmitter–receiver path. Furthermore, the size of the wave mixing zone can be precisely controlled

Table 1. Elastic parameters of the aluminum plate.

Set	λ (GPa)	μ (GPa)	$\bar{A}$ (GPa)	$\bar{B}$(GPa)	$\bar{C}$(GPa)
I	55.27	25.95	0	0	0
II	55.27	25.95	−351.2	−149.4	−102.8
III	55.27	25.95	−752.4	−298.8	−205.6
IV	55.27	25.95	−1053.6	−448.2	−308.4

by tuning the excitation cycles. Therefore, through tactically tuning the size of the wave mixing zone, damage detection can be carried out zone by zone to finally realize damage localization along the wave propagation path with only one transmitter–receiver pair, which can hardly be achieved by any existing guided-wave-based methods.

3. FE investigations

To verify the phenomena and understand the generation mechanism and the characteristics of the described mode-mixing-induced 2nd A0 waves, FE simulations are carried out using the model illustrated in figure 2. Taking advantage of the symmetric boundaries, only half of the model is used in simulations to reduce the computational cost. The sizes of the PZT, bonding layer and the aluminum plate used in the FE model are 5 mm × 0.3 mm, 5 mm × 0.03 mm and 600 mm × 2 mm, respectively. The PZT is modeled with the piezoelectric elements while the bonding layer and the plate are modeled with the plane strain elements. The guiding principle we used for choosing the maximum mesh size is to ensure a minimum of 20 elements per shortest wavelength of interest. In the current case, the mesh size for different components are 0.5 mm × 0.06 mm for the PZT, 0.5 mm × 0.006 mm for the bonding layer and 0.5 mm × 0.2 mm for the plate. The PZT and the bonding layer are treated as linear materials whose parameters can be found in our previous work [33]. The material parameters of the aluminum plate, in terms of the Lamé constants and the Landau third-order elastic constants, are listed in table 1. Four sets of parameters are used in the simulations to represent different health status of the plate. Specifically, Set-I represents pure linear aluminum and Set-II the intact aluminum with weak nonlinearity. As the higher order elastic constants are closely related to the material microstructures, the last two sets in the table are used for two aluminum materials containing incipient damage of increasing levels, from Set-III to Set-IV, which are taken from literature [34]. In addition, the plate is divided into four zones (A–D) where the material properties are selected from the four sets of material data in different simulations.

The first simulation focuses on the nonlinear wave phenomena. The whole plate is set as intact by attributing material Set-II to all four zones. The excitation is a pair of 5-cycle tone burst signals windowed by the Hann function at 100 kHz with inversed phases. It is worth noting that this frequency can be rather arbitrary. Since only material nonlinearity was considered in the numerical simulations, as long as the primary A0 and S0 waves can be effectively generated, the reported mixing will always take place. The amplitude of the excitation voltage on the PZT is 200 V. The out-of-plane displacements on the top and bottom surfaces of the plate at 300 mm from the origin are calculated. By superposing the two responses by the pair of excitations with inversed phase to eliminate the fundamental component [35], the second harmonic time-domain responses are extracted and shown in figure 3(a), showing two obvious wave packets in each response signal. According to the symmetric properties of the A0 and S0 mode Lamb waves, the first wave packet corresponds to the 2nd S0 wave indicated by the out-of-phase feature while the second one is associated with the 2nd A0 wave evidenced by the in-phase characteristic. This confirms the existence of the reported 2nd A0 wave.

The second simulation is then designed to validate the generation mechanism of the 2nd A0 wave. Zones A and B of the plate are assumed to be purely linear with the material Set-I. The remaining part is set to be intact with weak material nonlinearity with Set-II. Details of the wave excitation and sensing configurations are the same as those in the first simulation. This guarantees that the 1st S0 and 1st A0 mode Lamb waves only mix in the linear zone. The second harmonic out-of-plane displacement responses are extracted and shown in figure 3(b). Only the 2nd S0 mode waves exist in the responses. By comparing figures 3(a) and (b), it is clear that the 2nd A0 waves are generated due to the mode mixing of the 1st A0 and 1st S0 waves in the nonlinear plate.

The third simulation is designed to confirm the higher detectability of the 2nd A0 wave to local incipient damage. Zones B–D are set with the intact material Set-II while zone A is first set with the material Set II for the intact case and then Set-III and Set-IV for the damage cases. The excitation configurations remain identical to those in the previous two simulations. The second harmonic out-of-plane displacements on the top surface of the plate at 300 mm in the intact and damage cases are extracted and compared in figure 4(a). It can be seen that the amplitudes of both 2nd S0 and 2nd A0 waves increase from the intact case to the damage cases. By further extracting their amplitudes and carrying out the normalization to the intact case in figure 4(b), it is clear that the 2nd A0 wave are more sensitive to local incipient damage comparing to the commonly-used 2nd S0 wave if the damage locates in the mixing zone, as evidenced by the sharper increase in the 2nd A0 wave amplitudes. As mentioned before, this is because the 2nd A0 wave is induced by the material nonlinearity of the local wave mixing zone while the 2nd S0 wave contains the average damage information over the whole transmitter–receiver path.

The last simulation investigates the feasibility of using the 2nd A0 wave for damage localization. In the simulation, the central frequency of the excitations is kept at 100 kHz. The number of the tone burst cycles varies from 4 to 16 stepped by 2, which allows a tactic control of the size of the mode mixing zone. In this simulation, zone C is first assumed to be intact with material Set-II and then with the damaged material Set-IV. All other zones are set with the intact

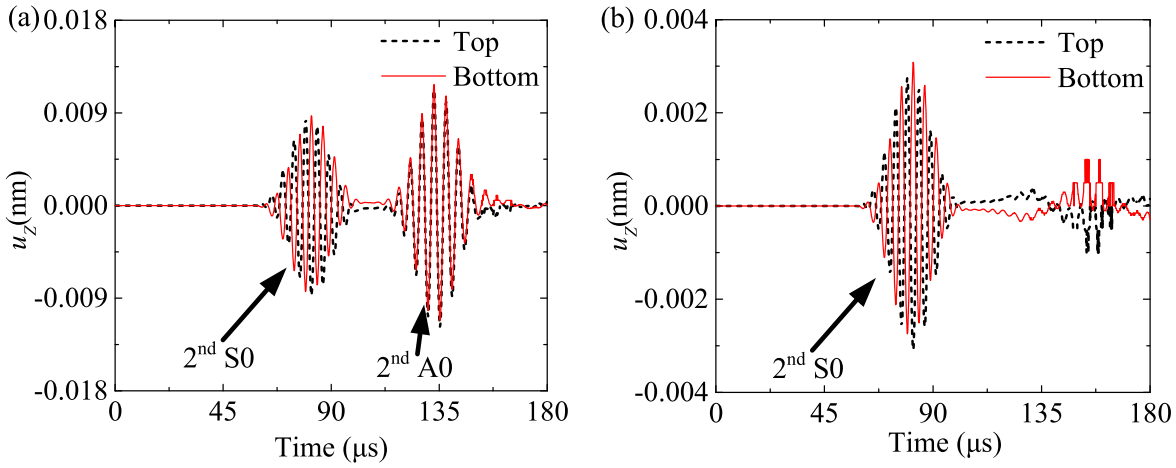

Figure 3. The second harmonic out-of-plane displacements at 300 mm on the top and bottom surfaces of the plate: (a) all the four zones set with Set-II; (b) zones A and B set with Set-I and zones C and D set with Set-II.

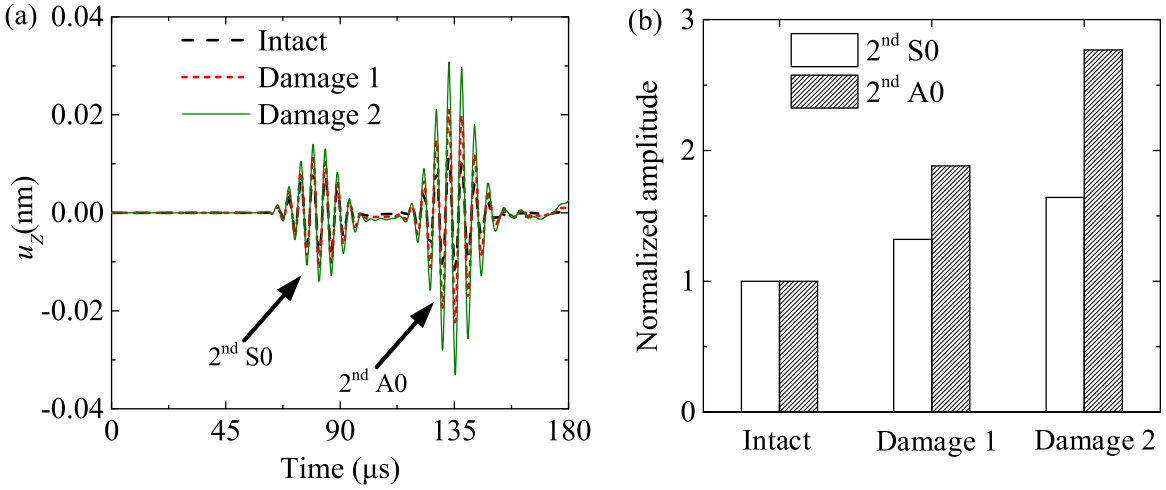

Figure 4. (a) The second harmonic out-of-plane displacements at 300 mm on the top surface of the plate in the intact and damage cases; (b) the normalized amplitude of the 2nd S0 and 2nd A0 waves.

material Set-II. The nonlinear out-of-plane displacements are extracted with the superposition method at 350 mm on the top surface of the plate. The second harmonic responses in two typical cases with 6-cycle and 12-cycle excitations are presented in figures 5(a) and (b), respectively. It can be seen from figure 5(a) that the amplitude of the 2nd S0 wave increases with the presence of damage while the 2nd A0 wave keeps almost unchanged. This is because mode mixing only occurs in the intact zone in this case. On the contrary, when the number of the excitation cycles increases to 12, the amplitudes of both the 2nd A0 and 2nd S0 mode increase from the intact case to the damage case as a result of mode mixing, also in the damage zone C. By further extracting the normalized amplitudes of the 2nd A0 and 2nd S0 waves in the damage cases with respect to the intact cases, results associated with different excitation cycles are shown in figure 5(c). Comparing to the 2nd S0 wave, the 2nd A0 wave is obviously more sensitive to the excitation cycles. Upon calculating the size of the mixing zone according to the excitation cycles, precise damage localization can eventually be realized, which will be realized in the following section. This simulation demonstrates the ability of the mode-mixing-induced 2nd A0 wave for damage localization using only one transmitter–receiver pair. It is also worth noting that the damage localization resolution can, in principle, be very high as the number of the excitation cycles can be tuned with small steps.

4. A dedicated damage localization algorithm

After demonstrating the potential of the 2nd A0 wave for incipient damage localization, a dedicated algorithm is further designed to achieve this goal for practical applications. Based on the generation mechanism of the mode-mixing-induced 2nd A0 wave, the proposed algorithm and the corresponding process are illustrated in figure 6 with the FE example as described in the previous section where a series of tone burst cycles N_i is adopted ($N_i = 4, 6, 8, 10, 12, 14, 16$ with i representing the ith excitation case). Recall that a damage localization can be theoretically realized by adjusting the duration of the excitation signals to tactically tune the size of the wave mixing zone. In the proposed algorithm, the first step is to evaluate the mixing

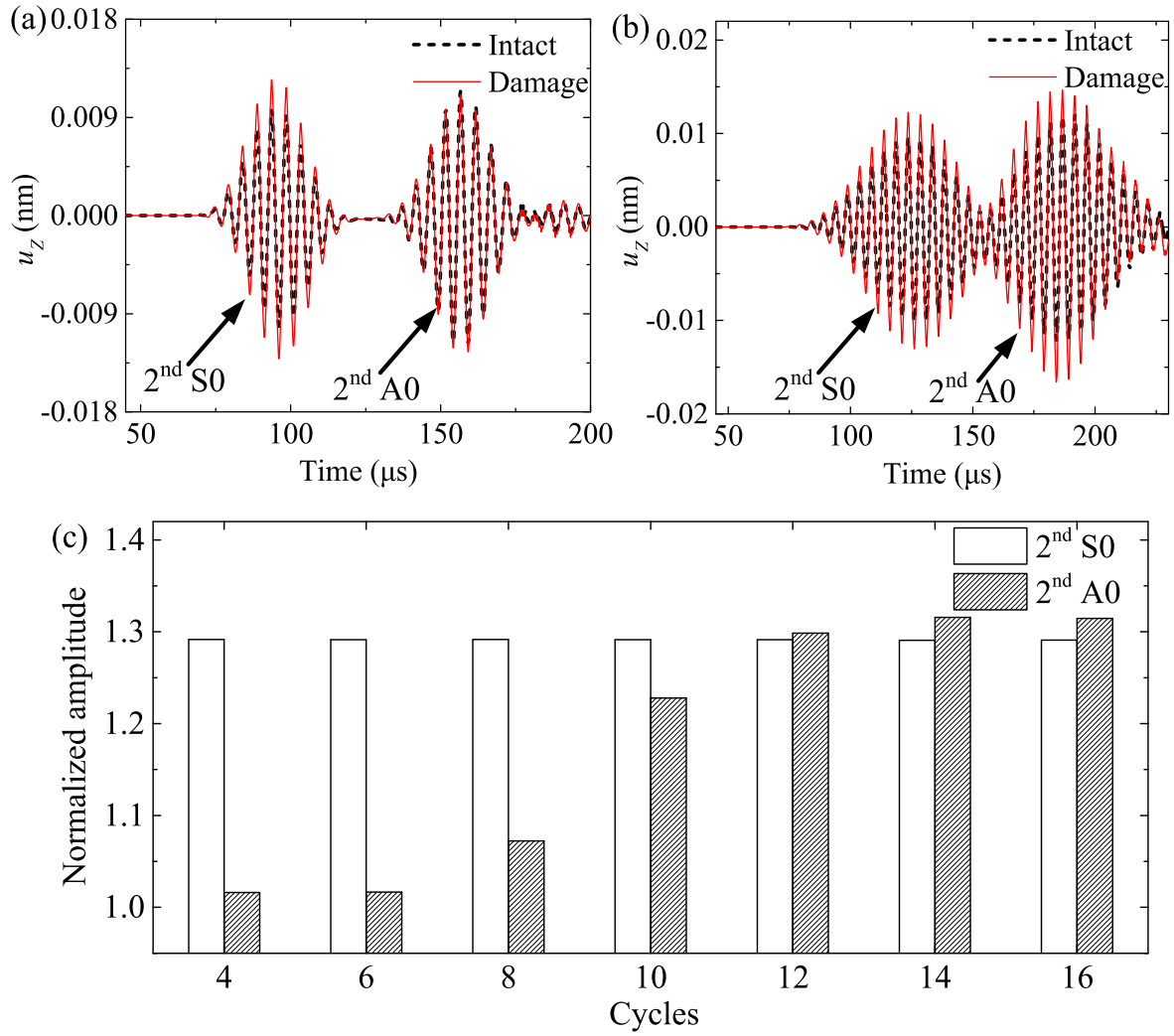

Figure 5. The second harmonic out-of-plane displacements at 350 mm on the top surface of the plate in the intact and damage cases associated with (a) 6-cycle excitations; (b) 12-cycle excitations; (c) the normalized 2nd A0 and 2nd S0 wave amplitudes associated with different number of excitation cycles.

zone of the primary S0 and A0 Lamb waves generated by a PZT actuator by introducing a mixing-zone estimation function (*MEF*) for a given excitation cycle N_i as

$$MEF(N_i, x) = \mathrm{Norm}\left(\int_0^{\infty} \mathrm{abs}(\mathrm{Hilbert}(S(N_i, x, t))) \cdot \mathrm{abs}(\mathrm{Hilbert}(A(N_i, x, t)))\mathrm{d}t\right). \quad (3)$$

$S(N_i, x, t)$ and $A(N_i, x, t)$ stand for the time-domain responses of the primary S0 and A0 mode Lamb waves at a certain position x away from the PZT actuator, respectively. The responses are calculated from the previously developed theoretical model which takes account of the dispersion of Lamb waves [28]. The operations abs(Hilbert()) and Norm() denote the envelop of a signal obtained from the Hilbert transform and normalization of a signal with respect to its maximum value, respectively. The *MEF*s in the specific FE example are plotted in figure 6(a) whose corresponding excitation cycles are marked with the numbers in the boxes.

Given two different excitation cases, e.g. N_i and N_{i-1} ($N_i > N_{i-1}$), the wave mixing zone for the N_{i-1}-cycle case should overlap with its counterpart for the N_i-cycle case. If directly using their *MEF*s for localization, damage information in the overlapped zone will be double-counted, as shown by the overlapped *MEF* at low values of x in the two cases in figure 6(a). To eliminate such effect, a zone determination function (*ZDF*) is proposed using the *MEF*s to define an effective zone for damage localization for the N_i-cycle case through comparison with its previous N_{i-1}-cycle case as

$$ZDF(N_i, x) = \begin{cases} MEF(N_1, x) & \text{for } i = 1 \\ \mathrm{Norm}\left(\dfrac{MEF(N_i, x)}{MEF(N_{i-1}, x)} - 1\right) & \text{for } i \geqslant 2 \end{cases}. \quad (4)$$

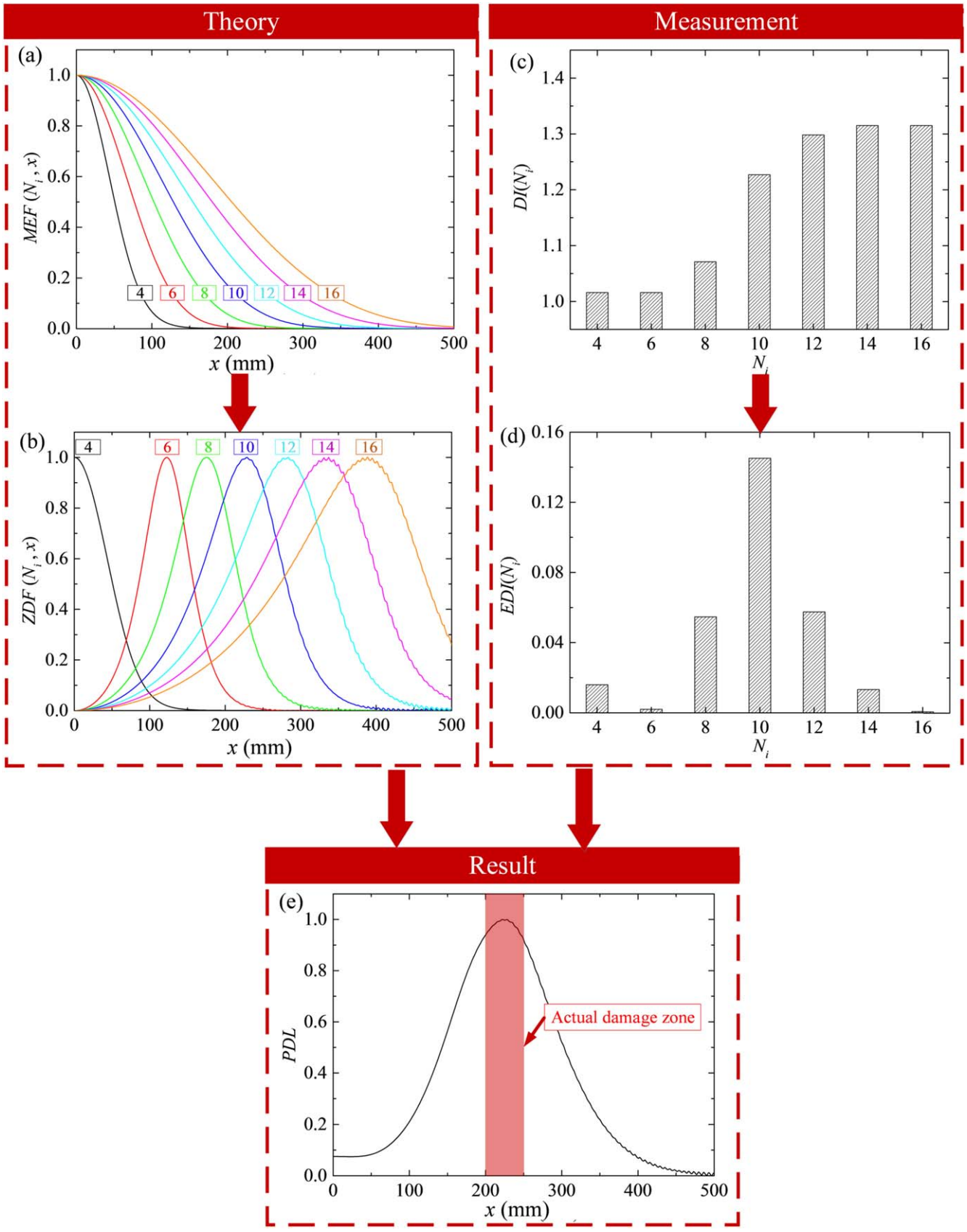

Figure 6. Process of the damage localization algorithm with an FE example detailed in the first part of the work[17]: (a) mixing-zone estimation function (*MEF*); (b) zone determination function (*ZDF*); (c) damage index (*DI*); (d) effective damage index (*EDI*); (e) possibility of damage localization (*PDL*).

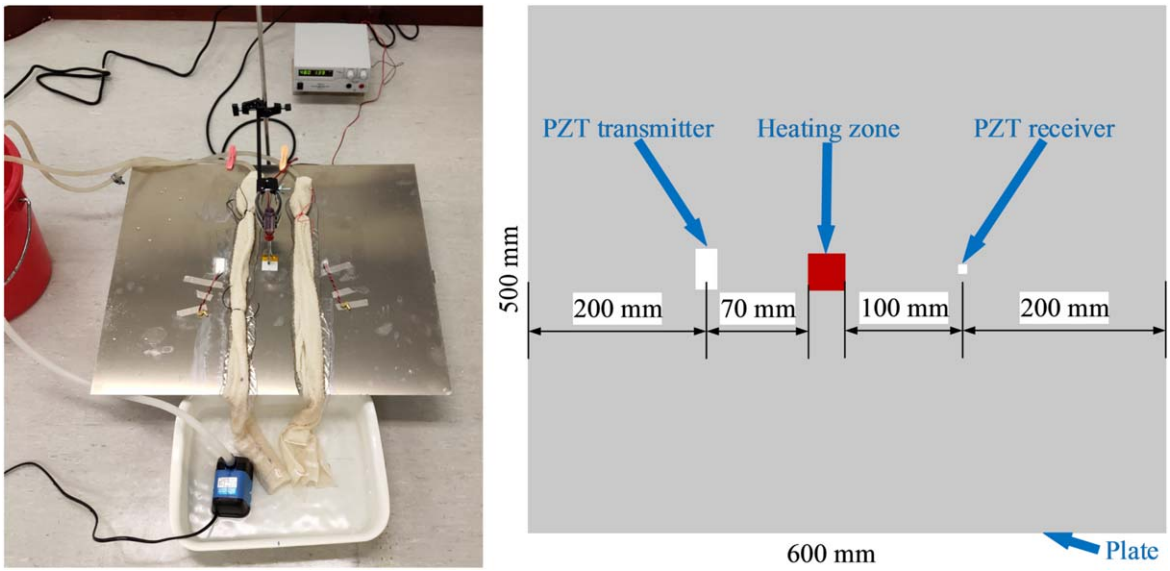

Figure 7. Experimental setup.

The *ZDF*s are calculated for the FE example and plotted in figure 6(b). With the proposed function, each excitation cycle case is responsible for a certain independent inspection zone with a likelihood distribution of damage localization.

After that, a damage index is defined based on the measurement results for a given excitation cycle case as

$$DI(N_i) = \frac{A_{test}(N_i)}{A_{baseline}(N_i)}, \tag{5}$$

where A_{test} and $A_{baseline}$ are the 2nd A0 wave amplitudes of the specimen under inspection and intact status, respectively. The *DI*s for different excitation cycles are obtained from FE simulation and shown in figure 6(c).

Based on the same principle as the definition of the *ZDF*, an effective damage index (*EDI*) is proposed accordingly as

$$EDI(N_i) = \begin{cases} DI(N_1) - 1 & \text{for } i = 1 \\ \dfrac{DI(N_i)}{DI(N_{i-1})} - 1 & \text{for } i \geqslant 2 \end{cases}. \tag{6}$$

The corresponding *EDI*s for the same FE example is shown in figure 6(d), which clearly shows a significant change when the excitation cycles vary from 8 to 10, which indicates the damage occurrence in the difference part of the mixing zones between the two excitation cases.

Finally, by synthesizing the *ZDF* from the theoretical analyses and the *EDI* from the test, the probability of damage localization (*PDL*) can be calculated by

$$PDL(x) = \mathrm{Norm}\left(\sum_{i=1}^{m} EDI(N_i) \cdot ZDF(N_i, x)\right). \tag{7}$$

Based on the above definition, the calculated *PDL* in the FE example is given in figure 6(e), which shows that the predicted damage localization result matches very well with the actual damage position, which validates the proposed algorithm.

It is worth noting that a high-resolution damage localization can, in principle, be achieved by refining the step of the excitation cycles. In addition, although the above detection strategy/algorithm is designed for the 2nd-A0-wave-based damage localization, the concept can be extended to other wave-mixing-based inspection techniques.

5. Experimental validations

Experiments are designed and conducted to confirm the existence of the reported 2nd A0 wave in a PZT-activated system on one hand, and to further assess the applicability of the proposed damage localization strategy/algorithm on the other hand. The experimental setup is illustrated in figure 7. Two PZTs are bonded using UHU 2-component epoxy on a 2024-T3 aluminum plate, as the transmitter (30 mm × 16 mm × 0.3 mm) and receiver (5 mm × 5 mm × 0.3 mm), respectively. In order to keep the consistency of the PZT installation, we use the same pressure to control the thickness of the bonding layer in different tests. The thickness of the bonding layer is measured with a micrometer through comparing the thickness changes before and after the epoxy is applied. In the present case, the thickness is around 0.03 mm. It is worth noting that apart from the incipient material nonlinearity of interest, other non-damage-related nonlinear sources like the adhesive nonlinearity (AN) from the bonding layer may also play a non-negligible role in the system, especially in the actuating part [33, 35], which might seriously jeopardize the operation if it is not properly apprehended. In this regard, the size of the transmitter is a result of a systematic system design based on our previous study [33], targeting a twofold objective: first, the primary S0 and A0 mode Lamb waves can be excited with high amplitude at around 140 kHz which is near the peaks of their corresponding frequency tuning curves; second, the non-damage-related adhesive linearities (AN) can be mitigated and reduced

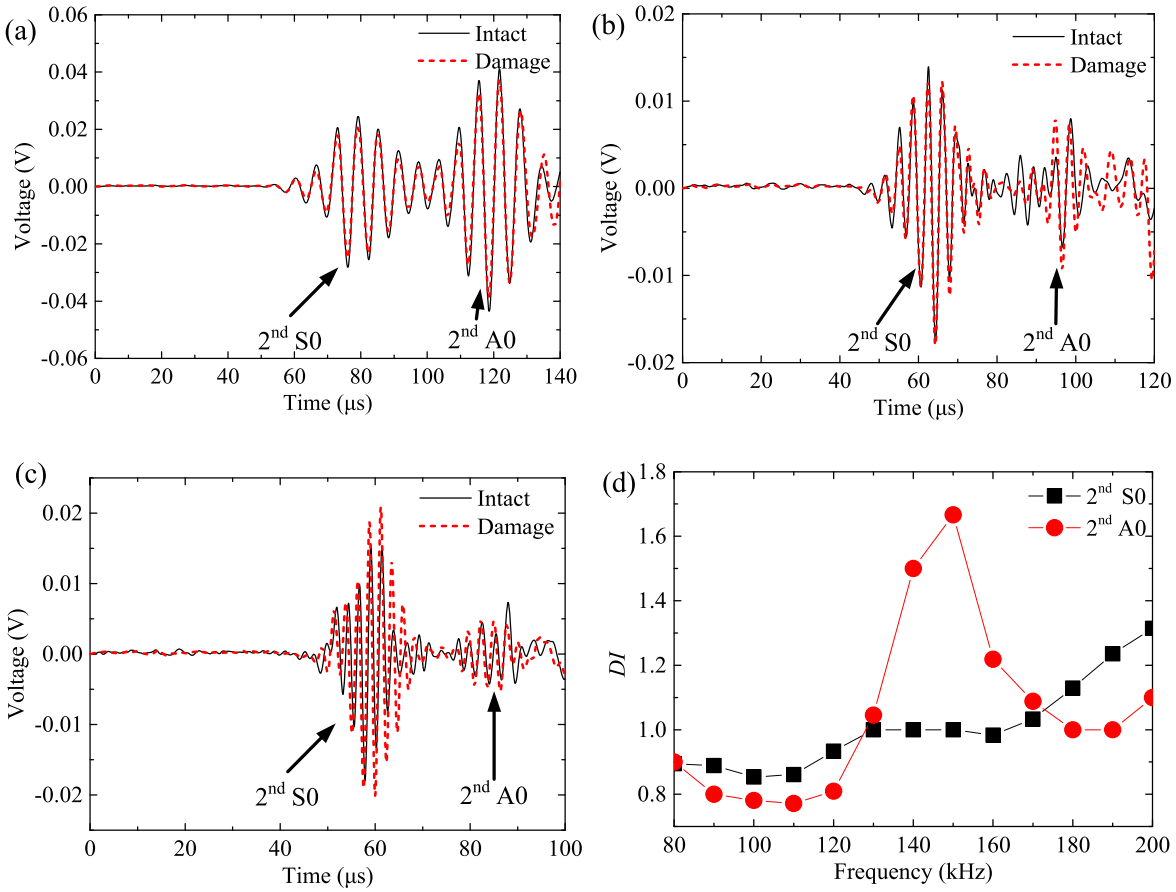

Figure 8. The second harmonic responses at different excitation frequencies before and after heating the plate with 6-cycle excitations: time-domain responses to (a) 60 kHz, (b) 140 kHz and (c) 200 kHz excitations respectively; (d) the DIs for both 2nd S0 and 2nd A0 waves.

to the lowest possible level at around 140 kHz for the 2nd A0 waves and at around 190 kHz for the 2nd S0 waves since the two frequencies locate near the valleys of the corresponding frequency tuning curves. A 30 mm × 30 mm metal ceramic heater is used to heat the plate for two hours to generate thermal changes inside the plate at different levels. The temperature on the heater surface can reach around 380 °C which is proven to be effective to entail a microstructural change inside the material [12, 33, 36]. Additionally, heat barriers with flowing water are installed to prevent the bonding layers and PZTs from being heated. The positions of the transducers and the heating zone are illustrated in figure 7.

Tests are first carried out with 6-cycle tone burst excitations windowed by the Hann function at different frequencies from 60 to 200 kHz step by 10 kHz. The measurement system, as well as the experimental process, can be referred to our previous work [35]. Within the frequency range of interest, the linear wave amplitudes change very slightly (less than ±3%) after the plate is heated (not shown here) so that they will be neglected in the following analyses. Then, a superposition method is adopted to extract the second harmonic wave components. The second harmonic responses from the intact and the heated plate in three typical cases are presented using three excitation frequencies: 60 kHz, 140 kHz, and 200 kHz respectively as shown in figures 8(a)–(c). It can be seen that both the 2nd S0 and A0 wave amplitudes hardly change at 60 kHz in figure 8(a). As to 140 kHz, the amplitude of the 2nd S0 wave slightly changes while that of the 2nd A0 wave increases significantly after the plate is heated. For the 200 kHz excitation case in figure 8(c), the 2nd S0 wave amplitude changes more obviously after the heating treatment than its 2nd A0 counterpart. Complex Morlet wavelet transform is further applied to extract the amplitudes of both 2nd S0 and A0 waves at different frequencies and the corresponding *DI*s are calculated and shown in figure 8(d) [37]. The largest *DIs* for the 2nd A0 and S0 waves can be found at around 150 kHz and 200 kHz respectively. This agrees with the theoretical predictions (140 kHz for the 2nd A0 wave and 190 kHz for the 2nd S0 wave) that non-damage-related AN is mitigated near the two frequencies for the corresponding second harmonic wave components. Since the heating-induced material microstructural changes can be characterized by the 2nd A0 wave, it evidently demonstrates the existence of the 2nd A0 wave induced by the material nonlinearity in the PZT-activated plate system. Moreover, through comparing the 2nd S0 and 2nd A0 results, it is found that the maximum *DI* for the 2nd A0 wave is about 1.7 while that for the 2nd S0 wave is around 1.3. This proves that the 2nd A0 wave indeed provides a higher detectability to local incipient damage than the 2nd S0 wave, also in agreement with the theoretical prediction.

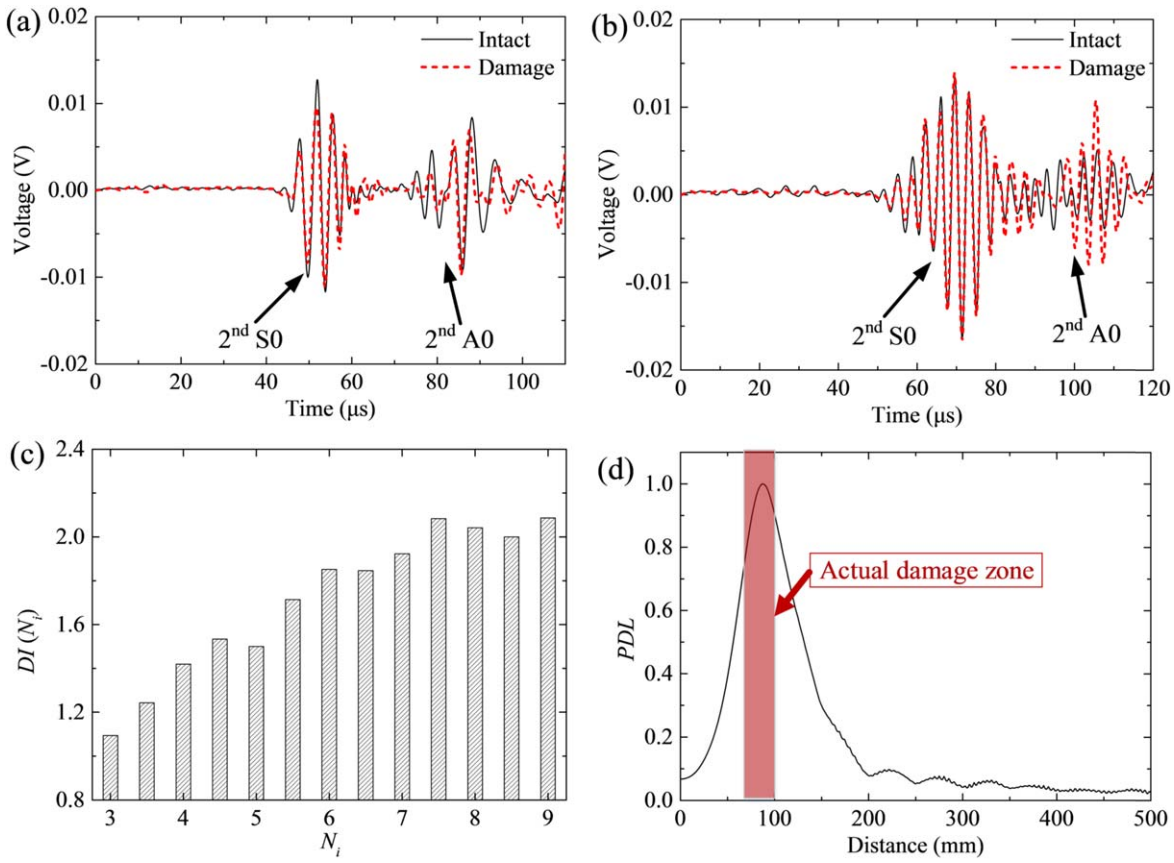

Figure 9. Damage localization based on the 2nd A0 waves at 140 kHz by adjusting the excitation cycles: (a) time-domain responses to 3-cycle excitations; (b) time-domain responses to 8-cycle excitations; (c) the DIs for 2nd A0 waves; (d) experimental result of the PDL.

Finally, by fixing the excitation frequency at 140 kHz, damage localization is carried out with the 2nd A0 wave by setting different wave excitation cycles from 3 to 9 stepped by 0.5. The second harmonic time-domain responses in two typical cases with 3 and 8 cycles are presented in figures 9(a) and (b). The amplitude changes of the 2nd A0 waves in the 8-cycle excitation case are much larger than that in the 3-cycle case. This is because the damage is outside the wave mixing zone for the 3-cycle excitation case but inside for the 8-cycle excitation case. After that, the *DI*s for different wave excitation cases are shown in figure 9(c), which shows a strong dependence of the *DI* on the wave excitation cycles, similar to the phenomenon observed in the FE studies. Finally, after obtaining the *EDI*s and *ZDF*s, the *PDL* can be finally calculated using experimental data and shown in figure 9(d). It can be seen that the predicted damage location agrees well with the actual damage position, thus experimentally validating the proposed damage localization strategy/algorithm in using the mode-mixing-induced 2nd A0 wave for incipient damage localization.

6. Conclusions

A special nonlinear wave phenomenon has been discovered as the mode-mixing-induced 2nd A0 waves in a PZT-activated damage inspection system. Its underlying mechanism is identified as the mode mixing of the 1st S0 and 1st A0 waves in a weakly nonlinear plate. FE simulations are carried out to ascertain this wave phenomenon and demonstrate its appealing characteristics for incipient damage detection and localization. A dedicated damage localization strategy/algorithm is proposed through synthesizing a theoretical model and measurements. Experiments are carried out by using a dedicatedly designed system with mitigated non-damage-related adhesive nonlinearities. Through locally heating a metal plate to create thermal induced material microstructural changes, the existence of the mode-mixing-induced 2nd A0 wave is confirmed. In addition, the 2nd A0 wave and the proposed damage localization algorithm are confirmed and validated in both FE and experimental perspectives.

Considering the characteristics of the primary S0 and A0 waves, the wave mixing zone is confined in a certain area surrounding the PZT actuator, which can be precisely controlled through changing the duration of the tone bust excitation cycle. This empowers the 2nd A0 wave with some appealing characteristics conducive to incipient damage inspection. First, the reported 2nd A0 wave exhibits a higher detectability to local incipient damage than the commonly used 2nd S0 wave resulting from the averaged/global material nonlinearity. Second,

high-resolution damage localization along the wave propagating path can be achieved with only one transmitter–receiver pair.

The findings of the present work are expected to contribute to the advancement of the nonlinear-guided-wave-based incipient damage inspection technique in several aspects. First, a special nonlinear wave phenomenon, new to the current state-of-art of the second harmonic generation, is discovered as the 2nd A0 wave, which provides an alternative tool for incipient damage inspection applications. Second, localization of incipient damage associated with material microstructural changes can be achieved, thus filling the gap left over by most of existing nonlinear-wave-based detection methods for damage localization. Third, the inspection system can be significantly simplified to realize high-resolution damage localization. Moreover, if using multiple sensors or a Laser Doppler Vibrometer for multi-position sensing, damage localization can be performed in a 2D pattern for the scanning of an inspection plane with only one fixed transmitter instead of an array and the required switching modules. Finally, although the present damage localization strategy/algorithm is designed for the present 2nd A0 wave case, the proposed concept can inspire the development of other wave-mixing-based methods for different damage localization applications.

Acknowledgments

The project was supported by grants from the Research Grants Council of Hong Kong Special Administrative Region (PolyU 152070/16E), the National Natural Science Foundations of China through SHENG project (Polish-Chinese Funding Initiative, 51961135302) and the Innovation and Technology Commission of the HKSAR Government to the Hong Kong Branch of National Rail Transit Electrification and Automation Engineering Technology Research Center.

ORCID iDs

Shengbo Shan https://orcid.org/0000-0002-0950-6193
Li Cheng https://orcid.org/0000-0001-6110-8099

References

[1] Chillara V K and Lissenden C J 2015 Review of nonlinear ultrasonic guided wave nondestructive evaluation: theory, numerics, and experiments *Opt. Eng.* **55** 011002
[2] Matlack K, Kim J Y, Jacobs L and Qu J 2015 Review of second harmonic generation measurement techniques for material state determination in metals *J. Nondestruct. Eval.* **34** 273
[3] Chillara V K and Lissenden C J 2015 On some aspects of material behavior relating microstructure and ultrasonic higher harmonic generation *Int. J. Eng. Sci.* **94** 59–70
[4] Lissenden C J, Liu Y and Rose J 2015 Use of non-linear ultrasonic guided waves for early damage detection *Insight, Non-Destr. Test. Cond. Monit.* **57** 206–11
[5] Mitra M and Gopalakrishnan S 2016 Guided wave based structural health monitoring: a review *Smart Mater. Struct.* **25** 053001
[6] Jhang K Y 2009 Nonlinear ultrasonic techniques for nondestructive assessment of micro damage in material: a review *Int. J. Precis. Eng. Manuf.* **10** 123–35
[7] Matsuda N and Biwa S 2011 Phase and group velocity matching for cumulative harmonic generation in Lamb waves *J. Appl. Phys.* **109** 094903
[8] Deng M 1999 Cumulative second-harmonic generation of Lamb-mode propagation in a solid plate *J. Appl. Phys.* **85** 3051–8
[9] Wan X, Tse P, Xu G, Tao T and Zhang Q 2016 Analytical and numerical studies of approximate phase velocity matching based nonlinear S0 mode Lamb waves for the detection of evenly distributed microstructural changes *Smart Mater. Struct.* **25** 045023
[10] Chillara V K and Lissenden C J 2012 Interaction of guided wave modes in isotropic weakly nonlinear elastic plates: higher harmonic generation *J. Appl. Phys.* **111** 124909
[11] Ishii Y, Biwa S and Adachi T 2018 Non-collinear interaction of guided elastic waves in an isotropic plate *J. Sound Vib.* **419** 390–404
[12] Hasanian M and Lissenden C J 2017 Second order harmonic guided wave mutual interactions in plate: Vector analysis, numerical simulation, and experimental results *J. Appl. Phys.* **122** 084901
[13] Sun M, Xiang Y, Deng M, Tang B, Zhu W and Xuan F 2019 Experimental and numerical investigations of nonlinear interaction of counter-propagating Lamb waves *Appl. Phys. Lett.* **114** 011902
[14] Metya A K, Tarafder S and Balasubramaniam K 2018 Nonlinear Lamb wave mixing for assessing localized deformation during creep *NDTE Int.* **98** 89–94
[15] Zhu W, Xiang Y, Liu C, Deng M and Xuan F 2018 A feasibility study on fatigue damage evaluation using nonlinear Lamb waves with group-velocity mismatching *Ultrasonics* **90** 18–22
[16] Sun X, Liu X, Liu Y, Hu N, Zhao Y, Ding X, Qin S, Zhang J, Zhang J and Liu F 2017 Simulations on monitoring and evaluation of plasticity-driven material damage based on second harmonic of S0 mode Lamb waves in metallic plates *Materials* **10** 827
[17] Masurkar F, Tse P and Yelve N P 2018 Evaluation of inherent and dislocation induced material nonlinearity in metallic plates using Lamb waves *Appl. Acoust.* **136** 76–85
[18] Zuo P, Zhou Y and Fan Z 2016 Numerical and experimental investigation of nonlinear ultrasonic Lamb waves at low frequency *Appl. Phys. Lett.* **109** 021902
[19] Packo P, Uhl T, Staszewski W J and Leamy M J 2016 Amplitude-dependent Lamb wave dispersion in nonlinear plates *J. Acoust. Soc. Am.* **140** 1319–31
[20] Zhu Y, Zeng X, Deng M, Han K and Gao D 2019 Mode selection of nonlinear Lamb wave based on approximate phase velocity matching *NDTE Int.* **102** 295–303
[21] Liu Y, Chillara V K and Lissenden C J 2013 On selection of primary modes for generation of strong internally resonant second harmonics in plate *J. Sound Vib.* **332** 4517–28
[22] De Lima W and Hamilton M 2003 Finite-amplitude waves in isotropic elastic plates *J. Sound Vib.* **265** 819–39
[23] Müller M F, Kim J Y, Qu J and Jacobs L J 2010 Characteristics of second harmonic generation of Lamb waves in nonlinear elastic plates *J. Acoust. Soc. Am.* **127** 2141–52
[24] Srivastava A and di Scalea F L 2009 On the existence of antisymmetric or symmetric Lamb waves at nonlinear higher harmonics *J. Sound Vib.* **323** 932–43
[25] Cho H, Hasanian M, Shan S and Lissenden C J 2019 Nonlinear guided wave technique for localized damage detection in plates with surface-bonded sensors to receive Lamb waves generated by shear-horizontal wave mixing *NDTE Int.* **102** 35–46

[26] Pruell C, Kim J Y, Qu J and Jacobs L J 2007 Evaluation of plasticity driven material damage using Lamb waves *Appl. Phys. Lett.* **91** 231911
[27] Pruell C, Kim J Y, Qu J and Jacobs L J 2009 Evaluation of fatigue damage using nonlinear guided waves *Smart Mater. Struct.* **18** 035003
[28] Xiang Y, Deng M and Xuan F 2014 Creep damage characterization using nonlinear ultrasonic guided wave method: a mesoscale model *J. Appl. Phys.* **115** 044914
[29] Xiang Y, Deng M, Xuan F and Liu C 2011 Experimental study of thermal degradation in ferritic Cr–Ni alloy steel plates using nonlinear Lamb waves *NDTE Int.* **44** 768–74
[30] Su Z and Ye L 2009 *Identification of Damage Using Lamb Waves: From Fundamentals to Applications* (London: Springer) (https://doi.org/0.1007/978-1-84882-784-4)
[31] Hong M, Su Z, Lu Y, Sohn H and Qing X 2015 Locating fatigue damage using temporal signal features of nonlinear Lamb waves *Mech. Syst. Signal Process.* **60** 182–97
[32] Boccardi S, Calla D B, Ciampa F and Meo M 2018 Nonlinear elastic multi-path reciprocal method for damage localisation in composite materials *Ultrasonics* **82** 239–45
[33] Shan S, Cheng L and Wen F 2018 Design of nonlinear-Lamb-wave-based structural health monitoring systems with mitigated adhesive nonlinearity *Smart Mater. Struct.* **27** 105006
[34] Choi G, Liu Y, Lissenden C J and Rose J 2014 Influence of localized microstructure evolution on second harmonic generation of guided waves *AIP Conf. Proc.* 1581, 631
[35] Shan S, Cheng L and Li P 2016 Adhesive nonlinearity in Lamb-wave-based structural health monitoring systems *Smart Mater. Struct.* **26** 025019
[36] Alexopoulos N D 2009 On the corrosion-induced mechanical degradation for different artificial aging conditions of 2024 aluminum alloy *Mater. Sci. Eng.* A **520** 40–8
[37] Shan S, Qiu J, Zhang C, Ji H and Cheng L 2016 Multi-damage localization on large complex structures through an extended delay-and-sum based method *Struct. Health Monit.* **15** 50–64